PCCP

COMMUNICATION

View Article Online
View Journal

Cite this: DOI: 10.1039/d5cp01709b

Received 6th May 2025,
Accepted 9th July 2025

DOI: 10.1039/d5cp01709b

rsc.li/pccp

Thermally activated delayed fluorescence in aminoacene-linked phenanthroline†

P. E. Swathi Krishna, Hanock Baiju and Mahesh Hariharan *

Twisted aminoacene D–A–D systems connected at the 2,9-position of phenanthroline were synthesized, showing thermally activated delayed blue fluorescence. Comprehensive computational and spectroscopic studies revealed hybrid localized and charge-transfer (HLCT) character, enabling reverse intersystem crossing, leading to delayed fluorescence.

Potential commercial applications in flat-panel displays and solid-state lighting have driven rapid advances in the development of viable organic light-emitting materials.[1–6] The two key processes that can ensure an increase in the efficiency of organic light-emitting chromophores by harvesting the triplet excitons are phosphorescence and thermally activated delayed fluorescence (TADF).[7,8] According to spin statistics, triplet excitons are formed three times more frequently than singlet excitons.[4] This hampers the light-emitting efficiency of organic light-emitting diodes (OLEDs) by less than 25%, as only singlet excitons are directly emissive.[4] At the outset, light-emitting efficiency has been improved by incorporating phosphors based on heavy metals like Ir(III), Pt(III), or Os(II), leading to enhanced intersystem crossing.[9] However, the expensive nature of heavy-metal-containing materials hinders their promising application in the fields of display technology and light generation.[9]

The synthetic modulation of organic chromophores has recently emerged to attain a hundred percent internal quantum efficiency by converting the triplet excitons back to singlet states by thermally activated reverse intersystem crossing (rISC), which results in delayed fluorescence emission.[10] The essential requirement to facilitate rISC is to decouple the highest occupied molecular orbital (HOMO) and the unoccupied molecular orbital (LUMO). The decoupled orbitals minimize overlap and thereby facilitate charge-transfer (CT) character and reduce the singlet–triplet energy gap.[11] However studies by Adachi and co-workers demonstrated that D–A–D systems with a singlet–triplet energy gap of more than 0.3 eV can also exhibit efficient blue TADF, with the mechanism involving reverse internal conversion (RIC) from a donor-centered $^3\pi\pi^*$ triplet state to the ^{3}CT state, followed by rISC to the emissive ^{1}CT state. The involvement of intermediate triplet states in the energy-transfer cascade underscores their critical role in enabling efficient delayed fluorescence in D–A–D architectures.[12] Herein, we describe a donor–acceptor–donor (D–A–D) system with aminoacenes as donors and a less-explored planar, rigid phenanthroline core as the acceptor, achieving a narrow photoluminescence spectrum and efficient blue thermally activated delayed fluorescence (TADF; Fig. 1a and b).

Molecules in the present study, BP and NP, were synthesized by the nucleophilic aromatic substitution (S_NAr) reaction of 2,9-dichloro-1,10-phenanthroline with aniline and 1-naphthylamine, respectively (Scheme S1, ESI†), following the reported procedure.[13] Subsequently, BP and NP single crystals were obtained from an ethyl acetate environment. BP and NP crystallized in centrosymmetric space groups $P2_1/n$ and C_2/c, respectively (Table S1, ESI†). Two asymmetric units were observed in both BP and NP crystal structures, with the latter containing a water molecule in the unit cell (Fig. 1c and d). The two asymmetric units in BP had minute variations in the torsional angles connecting the phenanthroline and benzene rings (Fig. S1, ESI†). However, in NP, naphthalene units were oriented in *syn*- and *anti*-conformations in the repeating unit (Fig. S2, ESI†). Weak non-covalent H···H and C···H interactions were major contributors towards herringbone-like three-dimensional packing in the crystals and were confirmed with the aid of Hirshfeld surface analysis (Tables S2, S3 and Fig. S3, ESI†).[14,15]

Both BP and NP exhibit distinct types of dimer in the crystal packing (Fig. S4 and S5, ESI†) that contribute towards three-dimensional packing. The interaction energy for various dimers is calculated using truncated symmetry-adapted perturbation theory (SAPT(0))-based energy decomposition analysis.[16] In the SAPT(0) method, the total interaction energy between two molecules is calculated by breaking it down into four energy

School of Chemistry, Indian Institute of Science Education and Research Thiruvananthapuram, Maruthamala P. O., Vithura, Thiruvananthapuram-695551, India. E-mail: mahesh@iisertvm.ac.in

† Electronic supplementary information (ESI) available. CCDC 2411806 and 2411807. For ESI and crystallographic data in CIF or other electronic format see DOI: https://doi.org/10.1039/d5cp01709b

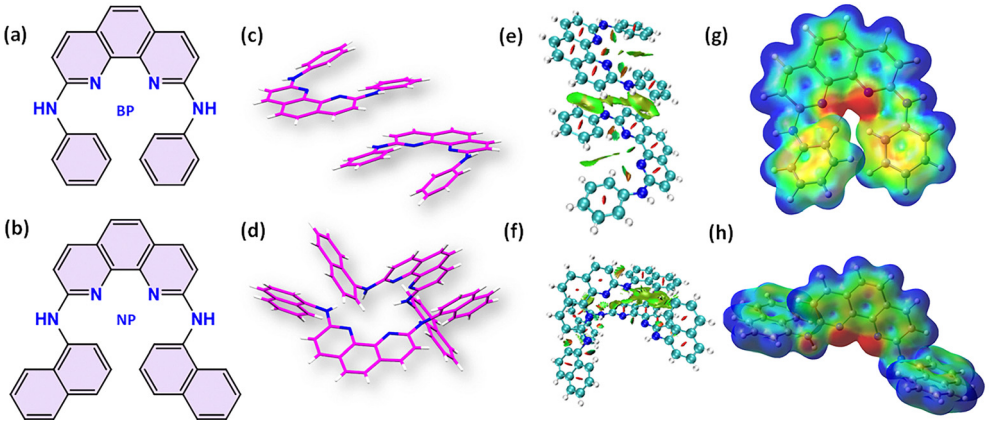

Fig. 1 Molecular structures of BP (a) and NP (b) with their crystal structures (c) and (d), respectively. NCI analysis of dimers of BP (e) and NP (f) in the crystal packing. Green discs and red discs represent stabilizing and destabilizing interactions, respectively. Electrostatic potential (ESP) surface generated for BP (g) and NP (h) with isovalue ±0.02 a.u. of electron density.

components: electrostatic, dispersion, induction, and exchange repulsion. Negative SAPT(0) values are obtained for all the dimers found in BP and NP crystals ($E_{SAPT(0)}$ = 0 to −30 kcal mol^{-1}), indicating that the above-mentioned interactions are stabilizing, contributing to the three-dimensional crystal packing (Tables S4 and S5, ESI†). A visual representation of the topology of electron density leading to non-covalent interaction in the various dimers contributing towards the crystal packing is obtained from non-covalent interaction analysis (NCI).[17] For the dimers in BP, both inter- and intramolecular H···H and C···H interactions in the NCI plot are indicated by green discs (Fig. 1e and Fig. S6, ESI†). Whereas for the dimers of NP, only intermolecular H···H and C···H interactions are obtained in the NCI plot (Fig. 1f and Fig. S7, ESI†).

As mentioned above, both BP and NP occupied two distinct conformations in the repeating unit of the crystal lattice. Electrostatic potential surface maps for two distinct monomers of both BP and NP revealed higher electron density near the nitrogen atoms of phenanthroline rings (Fig. 1g and h). In BP, the phenyl rings were aligned towards the center of the phenanthroline core, leading to a bulkier electronic distribution. However, in NP, the naphthalene units are oriented away from the phenanthroline backbone, reducing electron density. The excitonic coupling, mainly the Coulombic part, among the monomeric units of various dimers assimilated in BP and NP are computed using the electronic energy-transfer method available in Gaussian 16. The Coulombic interaction between the transition densities of various singlet states in the selected dimers of BP and NP is provided in Table S6 (ESI†). The Coulombic coupling values indicated for various dimers revealed weak to moderate intermolecular singlet–singlet coupling (100 cm^{-1} or less), and Coulombic energy transfer among lower BP and NP singlet states.

The UV-visible spectra of both BP and NP in toluene exhibited both n → π* and π → π* transitions ranging from 280 to 400 nm. Compared to 1,10-phenanthroline, the absorption spectra of both BP and NP are red-shifted by 100 nm by attachment of aminoacenes.[18] In the case of 1,10-phenanthroline, the absorption spectra have two intense peaks near 200 nm and 280 nm tailing towards 350 nm. However, in BP, the absorption spectra in toluene range up to 400 nm with two intense bands at 285 nm and 341 nm (Fig. S8, ESI†). The substitution of aminobenzene on the 2,9-positions of phenanthroline significantly altered the ground-state electronic properties. The UV-visible absorption spectra of NP also range up to 400 nm with an intense absorption band at 340 nm. When changing to naphthyl amine from benzene, there is insignificant variation in absorption maxima (Fig. S9, ESI†). On monitoring the fluorescence of BP and NP in toluene, the emission maxima (λ_F) are at 432 nm and 439 nm, with fluorescence quantum yields of φ_f = 0.038 and φ_f = 0.114 respectively. In comparison to 1,10-phenanthroline (λ_{max}^{emi} = 350 nm), the substitution of aminoacenes has resulted in a red-shift of 100 nm in the λ_{max}^{emi} of BP/NP with a significant increase in fluorescence quantum yield. Kubelka–Munk reflectance measurements were further carried out in single crystals of BP and NP arranged between quartz plates. The absorbance spectra in the crystalline state exhibited intense electronic transitions from 320 nm to 430 nm for both BP and NP (Fig. 2a and c). NP showed a weak absorption tail up to 600 nm. In the crystalline state, BP revealed an emission maximum λ_{max}^{emi} = 434 nm, with only a 2 nm shift compared to the monomeric state, indicative of weak excitonic coupling among individual molecules (Fig. S8, ESI†). On comparing the fluorescence spectra of BP in the crystalline state and toluene dielectric, the fluorescence intensity has a slight elevation of peak near 457 nm in crystals, as represented in Fig. S8 (ESI†). Similarly, NP in the crystalline state showed a 5 nm red-shift compared to the λ_{max}^{emi} monomeric solution state, possibly due to the insignificant electronic interaction among the monomers (Fig. S9, ESI†). The fluorescence microscope images of the crystals are provided in the inset (Fig. 2).

The monomers of BP and NP were optimized in the CAM-B3LYP/6-31G(d,p) level of theory. TD-DFT calculation yielded excited-state energy levels, as discussed in Tables S7 and S8 (ESI†). Upon analyzing the first few singlet excited states, both derivatives revealed almost negligible oscillator strength for the S_1 state. The S_1 state in both BP and NP systems exhibits significant energetic proximity to triplet states, potentially

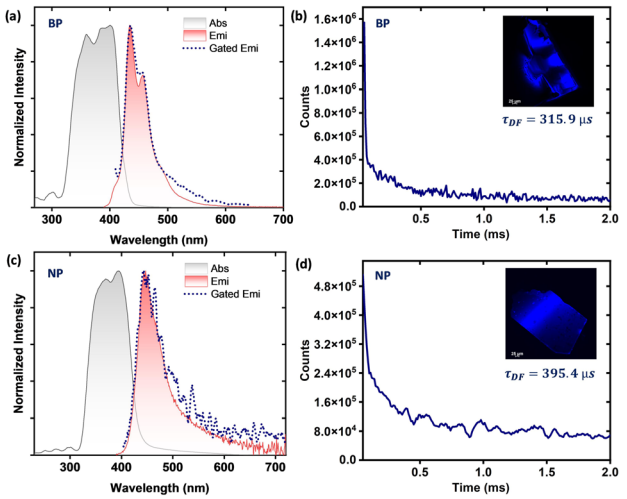

Fig. 2 The UV-Vis absorption spectra collected in diffuse reflectance mode along with fluorescence, gated emission spectra for (a) BP and (b) NP* (gating = 50 µs). *Baseline correction is performed on the gated emission of NP. The confocal fluorescence microscope images of crystals are provided in the inset.

facilitating reverse intersystem crossing (rISC) in the crystalline state. For BP, the T_5 state lies 157 meV below the S_1 state, whereas for NP, the T_6 state is 122 meV lower than the S_1 state, suggesting favorable energetics for triplet harvesting. Experimental measurements estimate the S_1–T_1 energy gap to be 610 meV for BP and 760 meV for NP. As rISC can proceed *via* higher-lying triplet states (T_n), these values may overestimate the energy gap that governs TADF. The calculated S_1–T_n gaps, more indicative of the thermally activated mechanism, are significantly smaller, 157 meV for BP and 122 meV for NP, supporting efficient triplet-to-singlet upconversion.[19]

The reduced singlet–triplet energy gap in the monomers of BP and NP motivated us to investigate the gated emission in the crystalline state. For BP and NP, the gated emission spectrum in the crystals overlaps with the corresponding fluorescence spectrum directed towards delayed fluorescence. The gated emission maxima are located at the corresponding λ_{max}^{emi} of BP and NP with a weak intense tail towards the red-edge. The lifetimes for the delayed fluorescence are measured by exciting BP at λ = 390 nm and collected at λ = 434 nm fitted to obtain τ_{DF} = 315.9 µs (Fig. 2b). In the case of NP, τ_{DF} = 395.4 µs is acquired by excitation at λ = 380 nm and collected at λ = 444 nm (Fig. 2d).

Further, a temperature-dependent gated measurement is performed in the crystalline state for BP and NP. For BP, at 77 K, gated emission spectra revealed multiple emission peaks, corresponding to delayed fluorescence and phosphorescence (Fig. S10a, ESI†). Upon fitting, the decays collected at a wavelength corresponding to the fluorescence maximum (λ_F = 429 nm) provided a very short lifetime within the pulse width (50 µs) (Fig. S11a, ESI†). However, upon increasing the temperature to 257 K, the lifetime also increased to τ_{DF} = 153.5 µs, confirming the presence of thermally activated delayed fluorescence in the crystalline state of BP (Table S9, ESI†). Apart from the emission peak at 429 nm, two new intense bands are observed near 450 nm and 520 nm at lower temperatures for BP. The lifetimes monitored at ~520 nm are also obtained from the decay curves (Fig. S11b–e, ESI†). The peak at 450 nm might be a combination of emission components from delayed fluorescence and phosphorescence.[20] In the case of BP, the partial charge-transfer nature of the triplet state resulted in a decrease in phosphorescence lifetime and intensity upon a rise in temperature, as indicated by the peak at ~520 nm. Thus, the emission band near 450 nm and 520 nm corresponds to phosphorescence in the crystalline state. In the case of NP, at 77 K, an emission maximum is observed corresponding to λ_F, indicating the possibility of delayed fluorescence (Fig. S10b, ESI†). Upon increasing the temperature from 77 K to 257 K, the fluorescence lifetime has increased from τ_{DF} = 91.4 µs to τ_{DF} = 387.5 µs, possibly due to thermal activation of delayed fluorescence in the crystalline state of NP (Table S10 and Fig. S12, ESI†). The photoluminescence intensity of NP decreased with increasing temperatures, which could be attributed to the activation of non-radiative decay processes.[21]

Additionally, gated measurements are performed in toluene solution at 77 K to support gated emission behaviour in the solid state. For BP, the spectra displayed an intense red-shifted peak corresponding to phosphorescence, along with a weaker peak near the emission maximum attributed to delayed emission. In the case of NP, a weak emission band was observed near λ_{max}^{emi} (Fig. S13, ESI†). Further investigation of delayed fluorescence properties in the amorphous state, within (i) a PMMA matrix and (ii) solution at room temperature, suggests that the delayed fluorescence is not predominantly governed by non-covalent interactions present in the crystalline phase (Fig. S14–S16, ESI†).

Natural transition orbitals are analyzed in the monomeric state to evaluate the nature of the observed TADF property in the crystals of BP and NP. For the two derivatives, for the S_1–S_0 transition, the hole is primarily delocalized across the entire molecular skeleton, while the electron is localized on the phenanthroline core. In contrast to conventional D–A–D systems with pronounced charge-transfer character, where the HUNTO is primarily localized on the donor units, the present system exhibits a notable acceptor contribution to the HUNTO. The molecular systems in the present study indicate partial electronic delocalization and conjugation between the donor and acceptor fragments.[22,23] The NTO plots show that the S_1–S_0 transition contains CT and LE components, as indicated by the overlap diagram (Fig. 3). To quantify the degree of charge transfer between different fragments in the molecular system the inter-fragment charge-transfer (IFCT) method is implemented. The IFCT method can be used to understand the extent of charge-transfer nature for a particular transition by separating the system into fragments. In the case of BP and NP, the phenanthroline core is taken as fragment-I and aminoacenes as fragment-II for computational evaluation. For the S_1–S_0 transition in BP, %CT = 31.01 and %LE = 68.99, while for NP, %CT = 26.73 and %LE = 73.27, implying hybrid local exciton and charge-transfer nature. Computational analysis using

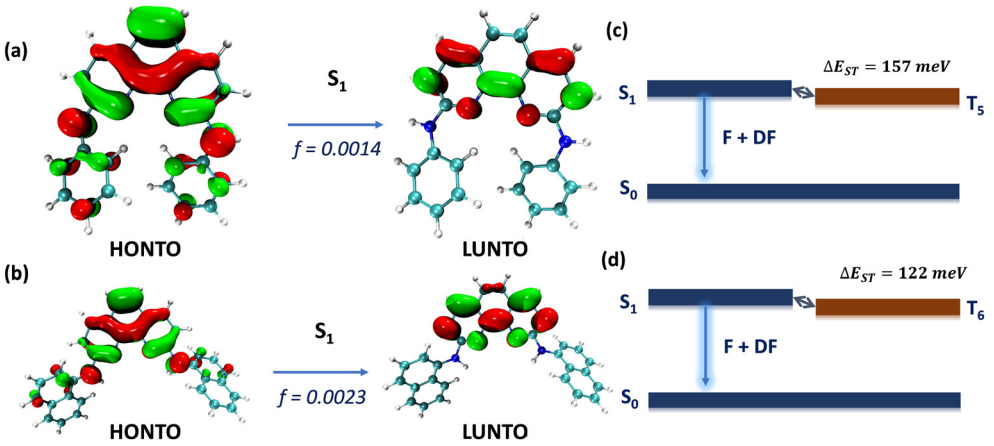

Fig. 3 NTO analysis for BP (a) and NP (b) in S_1 state. A schematic representation of a plausible mechanism TADF occurring in BP (c) and NP (d).

natural transition orbital (NTO) and intramolecular fragment charge-transfer (IFCT) methods suggests that the S_1 state tends to exhibit a hybridized nature, characterized as a hybrid local and charge-transfer (HLCT) state.

The nature of the transition to different singlet states is evaluated using the TheoDORE method.[24] In BP, the S_1 state exhibited CT = 0.386 (Table S11 and Fig. S17, ESI†) while in NP, the S_1 state shows borderline CT character (CT_{S1} = 0.373), confirming a state character in between LE and CT, plausibly contributing to delayed fluorescence properties (Table S12 and Fig. S18, ESI†). Solvent-dependent emission measurements revealed that BP exhibited minimal shifts in emission maxima (<5 nm), whereas NP showed a pronounced red-shift of 30 nm (Fig. S19, ESI†), indicating the partial charge-transfer character. The dipole moments of BP and NP were calculated in toluene, tetrahydrofuran and acetonitrile medium for the ground and first excited singlet state (Table S13, ESI†). The computationally evaluated dipole moments revealed insignificant solvatochromism for BP, but positive solvatochromism for NP.[25] The observed trend may arise from the enhanced electron-donating ability of the naphthylamino group and/or the significant variation in the donor–acceptor dihedral angle upon its incorporation.[26] The relatively small red-shift in BP suggests weak charge-transfer (CT) character, consistent with NTO and TheoDORE analyses.

Monkman and co-workers demonstrated that efficient TADF can occur even with large ΔE_{ST} (>0.3 eV) through involvement of an intermediate $^3n\pi^*$ state, facilitated by heteroatom-containing groups. The corresponding $^3n\pi^*$ state promotes efficient reverse intersystem crossing (rISC) to the ^{1}CT state. In our case, oxygen quenching experiments revealed a significant reduction in delayed emission intensity, supporting the involvement of triplet states (Fig. S14, ESI†). These observations suggest that a similar $^3n\pi^*$-mediated mechanism may be operative in our system, enabling efficient TADF despite a substantial singlet–triplet gap (Fig. 3c and d).[27]

In conclusion, we synthesized and crystallized two phenanthroline derivatives with benzene and naphthalene connected *via* an amino bridge behaving like a weak donor–acceptor–donor system with weak excitonic coupling. These heavy-atom-free organic chromophores exhibit thermally activated delayed fluorescence with a microsecond lifetime in their crystalline state with deep blue fluorescence. Computational analysis indicated that a combination of hybrid local excited and charge-transfer states modulates the delayed fluorescence behaviour. Our fundamental understanding of delayed fluorescence in the organic systems possibly paves the way for the material design of organic light-emitting diodes.

Conflicts of interest

There are no conflicts to declare.

Data availability

All the experimental data were provided in the ESI.†

Acknowledgements

M. H. acknowledges MoE-STARS/STARS-2/2023-0770 for financial support. S. K. P. E. acknowledges PMRF for financial assistance. We kindly thank Mr Alex P. Andrews for the X-ray diffraction analyses. We thank the Padmanabha HPC cluster at IISER TVM for the computing time.

Notes and references

1 H. Uoyama, K. Goushi, K. Shizu, H. Nomura and C. Adachi, *Nature*, 2012, **492**, 234–238.
2 K. Goushi, K. Yoshida, K. Sato and C. Adachi, *Nat. Photonics*, 2012, **6**, 253–258.
3 S. Feuillastre, M. Pauton, L. Gao, A. Desmarchelier, A. J. Riives, D. Prim, D. Tondelier, B. Geffroy, G. Muller, G. Clavier and G. Pieters, *J. Am. Chem. Soc.*, 2016, **138**, 3990–3993.
4 F. B. Dias, K. N. Bourdakos, V. Jankus, K. C. Moss, K. T. Kamtekar, V. Bhalla, J. Santos, M. R. Bryce and A. P. Monkman, *Adv. Mater.*, 2013, **25**, 3707–3714.

5 D. Zhang, L. Duan, C. Li, Y. Li, H. Li, D. Zhang and Y. Qiu, *Adv. Mater.*, 2014, **26**, 5050–5055.
6 H. Nakanotani, T. Higuchi, T. Furukawa, K. Masui, K. Morimoto, M. Numata, H. Tanaka, Y. Sagara, T. Yasuda and C. Adachi, *Nat. Commun.*, 2014, **5**, 4016.
7 Z. Yang, Z. Mao, Z. Xie, Y. Zhang, S. Liu, J. Zhao, J. Xu, Z. Chi and M. P. Aldred, *Chem. Soc. Rev.*, 2017, **46**, 915–1016.
8 Y. Tao, K. Yuan, T. Chen, P. Xu, H. Li, R. Chen, C. Zheng, L. Zhang and W. Huang, *Adv. Mater.*, 2014, **26**, 7931–7958.
9 M. E. T. M. A. Baldo and S. R. Forrest, *Organic Electroluminescence*, ed. Z. H. Kafafi, CRC press, Taylor & Francis Group, Boca Raton, 2005.
10 M. Y. Wong and E. Zysman-Colman, *Adv. Mater.*, 2017, **29**, 1605444.
11 K. Wu, T. Zhang, L. Zhan, C. Zhong, S. Gong, Z. H. Lu and C. Yang, *Adv. Opt. Mater.*, 2016, **4**, 1558–1566.
12 Q. Zhang, J. Li, K. Shizu, S. Huang, S. Hirata, H. Miyazaki and C. Adachi, *J. Am. Chem. Soc.*, 2012, **134**, 14706–14709.
13 T. Otani, A. Tsuyuki, T. Iwachi, S. Someya, K. Tateno, H. Kawai, T. Saito, K. S. Kanyiva and T. Shibata, *Angew. Chem., Int. Ed.*, 2017, **56**, 3906–3910.
14 M. A. Spackman and D. Jayatilaka, *CrystEngComm*, 2009, **11**, 19–32.
15 L. Loots and L. J. Barbour, *CrystEngComm*, 2011, **14**, 300–304.
16 K. Szalewicz, *Wiley Interdiscip. Rev.: Comput. Mol. Sci.*, 2012, **2**, 254–272.
17 J. Contreras-García, E. R. Johnson, S. Keinan, R. Chaudret, J. P. Piquemal, D. N. Beratan and W. Yang, *J. Chem. Theory Comput.*, 2011, **7**, 625–632.
18 G. Accorsi, A. Listorti, K. Yoosaf and N. Armaroli, *Chem. Soc. Rev.*, 2009, **38**, 1690–1700.
19 N. Uchida, T. Sato, J. Kuwabara, Y. Nishimura and T. Kanbara, *Chem. Lett.*, 2014, **43**, 459–461.
20 A. A. Kongasseri, S. Garain, S. N. Ansari, B. C. Garain, S. M. Wagalgave, U. Singh, S. K. Pati and S. J. George, *Chem. Mater.*, 2023, **35**, 7781–7788.
21 V. Ferraro, C. Bizzarri and S. Bräse, *Adv. Sci.*, 2024, **11**, 2404866.
22 M. Vasylieva, P. Pander, B. K. Sharma, A. M. Shaikh, R. M. Kamble, F. B. Dias, M. Czichy and P. Data, *Electrochim. Acta*, 2021, **384**, 138347.
23 R. Huang, J. Avó, T. Northey, E. Chaning-Pearce, P. L. dos Santos, J. S. Ward, P. Data, M. K. Etherington, M. A. Fox, T. J. Penfold, M. N. Berberan-Santos, J. C. Lima, M. R. Bryce and F. B. Dias, *J. Mater. Chem. C*, 2017, **5**, 6269–6280.
24 F. Plasser, *J. Chem. Phys.*, 2020, **152**, 84108.
25 C. Reichardt, *Chem. Rev.*, 1994, **94**, 2319–2358.
26 A. Dreuw and P. Tegeder, *Phys. Chem. Chem. Phys.*, 2023, **25**, 17079–17091.
27 F. B. Dias, J. Santos, D. R. Graves, P. Data, R. S. Nobuyasu, M. A. Fox, A. S. Batsanov, T. Palmeira, M. N. Berberan-Santos, M. R. Bryce and A. P. Monkman, *Adv. Sci.*, 2016, **3**, 1–10.